Deformed neutron halos with shape decoupling in neutron-rich magnesium isotopes

Yu-Xuan Luo,[1] Quan Liu,[2,*] Xue-An Pan,[3] Xiao Chang,[1] and Jian-You Guo[2]

[1]*School of Electronic and Information Engineering,*
Hefei Institute of Technology, Hefei 238076, China
[2]*School of physics and Optoelectronic Engineering, Anhui University, Hefei 230601, China*
[3]*School of Physics and Materials Engineering, Hefei Normal University, Hefei, 230601, China*

(Dated: April 23, 2026)

Background: The exploration of neutron-rich nuclei far from stability has revealed exotic phenomena like the change of magic numbers, shape coexistence, and halo formation. Neutron-rich magnesium isotopes provide a pivotal testing ground for understanding how shell evolution, deformation, and continuum coupling collectively govern nuclear structure near the drip line.

Purpose: This work aims to systematically investigate the ground-state properties and the emergence of deformed neutron halos in even-even magnesium isotopes $^{34-44}$Mg, with a focus on the microscopic mechanisms driving shell closure quenching, deformation development, and halo formation.

Methods: We employ the deformed relativistic mean-field theory combined with the complex momentum representation and BCS pairing (DRMF-CMR-BCS). This framework self-consistently treats deformation, pairing correlations, and continuum coupling, providing a unified description of bound, resonant, and continuum states. Calculations are performed using the NL3 effective interaction.

Results: Our calculations reveal the microscopic mechanism for the collapse of the $N = 20$ and $N = 28$ shell closures, identifying it as a cooperation of monopole drift in key neutron orbitals (e.g., $1/2_1^-$, $3/2_2^-$) and the stabilization of prolate deformation. In ^{40,42,44}Mg, we predict the universal emergence of deformed halos characterized by a striking shape decoupling: a prolate core coexists with an oblate halo. This halo is predominantly formed by low-angular-momentum orbitals, with the dominant contributor shifting from a narrow resonant state ($3/2_2^-$) in ^{40}Mg to a weakly bound orbital ($3/2_2^-$) in ^{42}Mg. The anomalous occupancy of narrow resonances underscores the important role of pairing, enhanced continuum coupling.

Conclusions: The structure of neutron-rich Mg isotopes is governed by the intricate competition between single-particle energies, deformation, pairing, and the continuum. Our calculations offer clear, testable predictions for future rare-isotope beam experiments.

I. INTRODUCTION

The advent of next-generation radioactive beam facilities, such as RIKEN, FRIB, GSI, and HIRFL, coupled with advanced detection systems, has opened unprecedented opportunities to explore exotic nuclei far from the β-stability line. These frontier experiments have revealed a wealth of novel nuclear phenomena, including the modification of magic numbers [1], shape coexistence [2–4], energy-level inversion [5, 6], and halo structures [7, 8]. Such discoveries fundamentally challenge our understanding of nuclear many-body systems and call for advanced theoretical frameworks that can account for the unique properties of weakly bound nuclei.

The emergence of these exotic phenomena is governed by the intrinsic nature of single-particle states near the Fermi surface and their coupling to the continuum. In nuclei with extreme neutron-to-proton ratios, the Fermi energy lies close to the particle-emission threshold, placing valence nucleons in proximity to unbound configurations. Residual interactions, particularly pairing correlations, can scatter nucleon pairs into the continuum, making the role of continuum effects, including resonant states-essential for a comprehensive description of exotic nuclear structure [9, 10].

Single-particle resonant states play a pivotal role in this context. A variety of theoretical tools have been developed to probe these states, including the R-matrix [11, 12], K-matrix [13], analytic continuation in the coupling constant [14], Green's function [15–17], scattering phase shift (SPS) [18–20], and complex scaling methods [21]. For light nuclei, *ab initio* methods such as the No-Core Shell Model(NCSM) [22] and Green's Function Monte Carlo (GFMC) method [23] have achieved remarkable success, while the Coupled Cluster Method (C-CM) [24] has extended such calculations toward heavier drip-line nuclei. To address deformation and continuum effects in exotic nuclei, the deformed relativistic Hartree-Bogoliubov in continuum (DRHBc) model [25, 26] employs coordinate-space Woods-Saxon wave functions as a basis and incorporates pairing via Bogoliubov quasiparticle transformations, thereby self-consistently treating deformation, continuum coupling, and pairing correlations.

A powerful alternative for describing exotic nuclear structure is the complex momentum representation (CM-R) method, which uniformly treats bound, resonant, and continuum states. The Berggren completeness relation within CMR combines these states while avoiding the artificial confinement of harmonic oscillator bases and the numerical complexities of direct coordinate-space cal-

---

[*] E-mail:quanliu@ahu.edu.cn

culations. Based on CMR, the Gamow Shell Model (GSM) has shown promising results [27, 28], and the Gamow-Hartree-Fock-Bogoliubov method [29] has successfully described medium-mass to heavy exotic nuclei, highlighting the important role of CMR in advancing non-relativistic nuclear energy density functionals.

The relativistic mean field (RMF) theory stands as a cornerstone of microscopic nuclear models, providing both self-consistent spin-orbit potentials-accounting for pseudospin symmetry-and accurate descriptions of stable and exotic nuclei [30]. By combining CMR with RMF, we established the RMF-CMR theory, which resolves single-particle resonances in spherical nuclei, including broad, low-angular-momentum resonances inaccessible to conventional methods [31–33]. To address pairing and continuum coupling, we incorporated Bardeen-Cooper-Schrieffer (BCS) theory, developing the RMF-CMR-BCS approach for spherical nuclei, which successfully explained halo and giant halo phenomena [34–36]. Recognizing the universality of deformation, we extended the relativistic CMR method to deformed nuclei by solving the Dirac equation in a phenomenological Woods-Saxon potential [37–39]. More recently, we combined CMR with deformed relativistic mean-field (DRMF) theory and BCS pairing to establish the DRMF-CMR-BCS theory, which we applied to deformed systems. This approach has revealed the deformed halo structure in ^{44}Mg [40] and the ground-state properties of neutron-rich sodium isotopes [41], establishing the decisive role of resonant states in halo formation.

Magnesium isotopes have garnered significant attention due to their rich structural phenomena, including the “island of inversion”, shape coexistence, halo formation, deformation effects in halo nuclei, and shell evolution. In the neutron number range $N = 20 - 28$, these isotopes exhibit dramatic shell evolution marked by the collapse of shell closures, novel mechanisms of shape coexistence, and the quenching of magic numbers.

Significant breakthroughs in understanding the shell evolution of magnesium isotopes have emerged from the cooperation between radioactive ion beam experiments and many-body theoretical approaches. Experimental observations disclosed the collapse of the $N = 20$ shell closure in ^{28,29}Mg, linked to intruder orbital configurations [42, 43]. Compelling evidence comes from ^{32}Mg, where the low-lying first excited 2^+ state at 885 keV and small quadrupole deformation ($\beta_2 = 0.25$) [44], combined with direct mass measurements revealing a reduced neutron gap near $N = 20$ [45], signaled a dramatic modification of shell structure. The case of ^{30}Mg exhibits shape coexistence, with the ground state maintaining the traditional sd-shell ($0p$-$0h$) configuration while excited states adopt deformed $2p$-$2h$ intruder configurations [46].

β^--decay experiments [4] unambiguously identified the ground state of ^{31}Mg as a deformed intruder configuration with significant prolate deformation, challenging traditional shell-model boundaries. The 0^+ excited states in ^{32}Mg show remarkable configuration coexistence, as revealed by two-neutron transfer reactions indicating multi-particle excitations across the sd-fp shell [47]. In ^{33}Mg, both the ground state ($3/2^-$) and low-lying excited state ($5/2^-$) exhibit enhanced occupation of the $2p_{3/2}$ orbital, indicating deformation driven by intruder configurations [48, 49]. Systematic β-decay spectroscopy has shown that this structural evolution is driven by $1p$-$1h$ and $2p$-$2h$ excitations [49, 50], while nucleon knockout reactions have uncovered significant multi-particle-hole excitations in the ground state of ^{33}Mg, with quadrupole deformation exceeding conventional shell-model predictions [51]. The electric dipole response in ^{33}Mg revealed collective excitations exceeding $3p$-$3h$ configurations in its ground state [52], challenging spherical model predictions. The large quadrupole deformation ($\beta_2 = 0.58$) and enhanced $B(E2)$ value in ^{34}Mg disclose pronounced collective behavior beyond standard sd-shell model predictions [53, 54].

The energy of the 2_1^+ state in ^{36}Mg drops strikingly to 660(6) KeV, confirming the deformation-driven role of sd-fp shell mixing [55]. This observation directly demonstrates the significant quenching of closed-shell effects as neutrons approach $N = 28$ [56]. The first observation of the 2^+ state in ^{40}Mg confirms the complete collapse of the $N = 28$ shell closure in extreme neutron-rich regions [57]. These findings establish that suppressed shell closures are widespread and exhibit a common effect with the weakening of the $N = 20$ shell closure. Shell-model calculations have shown that such shell quenching can lead to the expansion of traditional shell boundaries toward the neutron drip line [58]. This mechanism universally explains the coexistence of intruder states (e.g., $2p_{3/2}$ occupation) and normal spherical configurations, as well as the enhanced many-body correlations driving nuclear deformation.

Significant progress has also been made in identifying exotic structures in magnesium isotopes. The heaviest known halo nucleus, ^{37}Mg, was unambiguously identified through its large reaction cross section and distinctive intruder orbital configuration [59, 60]. RMF calculations indicate that the neutron Fermi surface in ^{40}Mg approaches the continuum threshold, suggesting exotic halo features [61]. Notably, the neutron density distribution in ^{40}Mg decouples from the core in excited states, demonstrating the stability of deformed halo structures during collective rotation [62]. DRHB theory predicts substantial ground-state deformation ($\beta_2 = 0.32$) in ^{44}Mg, with notable core quadrupole deformation [25]. The predicted neutron halo in ^{44}Mg arises mainly from the occupation of classically forbidden orbitals [63]. Studies of ^{42}Mg and ^{44}Mg reveal pronounced spatial extensions in pairing density distributions, with a positive correlation between surface deformation and neutron halo diffuseness. Hyperspherical harmonic expansion calculations confirm that the deformation parameters of low-lying states in ^{42}Mg and ^{44}Mg remain large while exhibiting neutron density decoupling from the core [64], in excellent agreement with the Bohr-Mottelson model of collective motion for deformed nuclei [65].

The DRMF-CMR-BCS method employed in the present work directly treats bound, resonant, and continuum states on an equal footing, enabling a clear identification of resonance parameters (energies and widths) from the eigenvalue problem in the complex momentum plane. Unlike our previous work on ^{44}Mg [40], which focused on a single isotope, the present study provides a systematic investigation of six even-even magnesium isotopes from ^{34}Mg to ^{44}Mg. This expanded scope allows us to reveal the evolution of shell structures, deformation, and halo formation in neutron-rich magnesium isotopes. We perform multipole decomposition of the core and halo densities to quantitatively establish the shape decoupling phenomenon, a prolate core coexisting with an oblate halo, as a general feature in deformed neutron-rich magnesium isotopes. We also discuss the systematic evolution of halo formation mechanisms across isotopes, where the dominant contributor shifts from a narrow resonant state in ^{40}Mg to a weakly bound orbital in ^{42}Mg. The theoretical formalism is presented in Sec. II. In Sec. III, we provide numerical details and results for the even-even nuclei $^{34-44}$Mg. A summary is given in Sec. IV.

II. FORMALISM

To analyze the structure of exotic nuclei, we introduce the DRMF-CMR-BCS theoretical framework. Starting with the RMF approach [9, 66, 67], this formalism treats nucleons as Dirac particles with interactions mediated by photons and mesons. The governing Lagrangian density is defined as follows:

$$\begin{aligned}\mathcal{L} = & \bar{\psi}[i\gamma^{\mu}\partial_{\mu} - M - g_{\sigma}\sigma - g_{\omega}\gamma^{\mu}\omega_{\mu} - g_{\rho}\gamma^{\mu}\vec{\tau}\vec{\rho}_{\mu}]\psi \\ & -\bar{\psi}[\frac{1}{2}e\gamma^{\mu}(1-\tau_3)A_{\mu}]\psi + \frac{1}{2}(\partial_{\mu}\sigma\partial^{\mu}\sigma - m_{\sigma}^2\sigma^2) \\ & -\frac{1}{4}\omega^{\mu\nu}\omega_{\mu\nu} + \frac{1}{2}m_{\omega}^2\omega^{\mu}\omega_{\mu} - \frac{1}{3}g_2\sigma^3 - \frac{1}{4}g_3\sigma^4 \\ & -\frac{1}{4}\vec{\rho}^{\mu\nu}\vec{\rho}_{\mu\nu} + \frac{1}{2}m_{\rho}^2\vec{\rho}^{\mu}\vec{\rho}_{\mu} + \frac{1}{4}c_3(\omega^{\mu}\omega_{\mu})^2 \\ & -\frac{1}{4}F^{\mu\nu}F_{\mu\nu}. \end{aligned} \tag{1}$$

The coupling constants g_{ω}, g_{σ}, and g_{ρ} correspond to the isoscalar-vector ω, isoscalar-scalar σ, and isovector-vector ρ mesons, respectively. Their associated masses are m_{ω}, m_{σ}, and m_{ρ}. The Dirac equation for nucleon motion emerges from the classical variational formalism,

$$[\vec{\alpha}\cdot\vec{p} + \beta\,(M+S) + V]\,\psi = \varepsilon_i\psi. \tag{2}$$

where the scalar and vector potentials of nucleons $S\,(\vec{r}) = g_{\sigma}\sigma\,(\vec{r})$, $V\,(\vec{r}) = g_{\omega}\omega^0\,(\vec{r}) + g_{\rho}\tau_3\rho^0\,(\vec{r}) + eA^0\,(\vec{r})$. The Klein-Gordon equations for the meson fields are given in Refs. [9, 66, 67], as well as the density terms for mesons and photons

$$\begin{aligned}\rho_s &= \sum_{i=1}^{A}\bar{\psi}_i\psi_i, \rho_v = \sum_{i=1}^{A}\psi_i^{\dagger}\psi_i, \\ \rho_3 &= \sum_{i=1}^{A}\psi_i^{\dagger}\tau_3\psi_i, \rho_c = \sum_{p=1}^{Z}\psi_p^{\dagger}\psi_p. \end{aligned} \tag{3}$$

In axisymmetric systems, π (parity) and m_j (the third component of total angular momentum) serve as good quantum numbers. The Dirac spinor can be decomposed via a spherical harmonic basis:

$$\psi_{m_j}(\vec{r}) = \frac{1}{r}\sum_{lj}\begin{pmatrix} iG^{lj}(r)Y_{jm_j}^{l}\,(\Omega_r) \\ -F^{lj}(r)Y_{jm_j}^{\tilde{l}}\,(\Omega_r) \end{pmatrix}, \tag{4}$$

defining $\tilde{l} = 2j - l$, and using the spin spherical harmonics $Y_{jm_j}^{l}\,(\Omega_r)$, the scalar and vector densities are derived by inserting Eq. (4) into Eq. (3). Their radial dependencies are given by:

$$\rho_s(r,\theta) = \sum_{\lambda}\frac{2\lambda+1}{4\pi r^2}P_{\lambda}(\cos\theta)\sum_{i(lj)(lj)'}\nu_i^2\left(G_i^{lj}G_i^{(lj)'} - F_i^{lj}F_i^{(lj)'}\right)A\left(\lambda,(lj)',(lj),m_j\right), \tag{5}$$

$$\rho_{\nu}(r,\theta) = \sum_{\lambda}\frac{2\lambda+1}{4\pi r^2}P_{\lambda}(\cos\theta)\sum_{i(lj)(lj)'}\nu_i^2\left(G_i^{lj}G_i^{(lj)'} + F_i^{lj}F_i^{(lj)'}\right)A\left(\lambda,(lj)',(lj),m_j\right), \tag{6}$$

with

$$A\left(\lambda,(lj)',(lj),m_j\right) = \int d\Omega Y_{jm_j}^{l}(\cos\theta)^{*}P_{\lambda}(\cos\theta)Y_{j'm_j}^{l'}(\cos\theta) = \int d\Omega Y_{jm_j}^{\tilde{l}}(\cos\theta)^{*}P_{\lambda}(\cos\theta)Y_{j'm_j}^{\tilde{l}'}(\cos\theta), \lambda = 0,2,4,\ldots$$

The Dirac equation (Eq. (2)) and the Klein-Gordon equations for the meson fields comprise a set of coupled equations, which are solved numerically via iterative methods under prescribed precision. Resonant states are derived by transitioning the Dirac equation (2) to momentum space,

$$\int d\vec{k}' \left\langle \vec{k} \right| H \left| \vec{k}' \right\rangle \psi(\vec{k}') = \varepsilon \psi(\vec{k}). \tag{7}$$

Here, $H = \vec{\alpha} \cdot \vec{p} + \beta \left(M + S\left(\vec{r}\right)\right) + V\left(\vec{r}\right)$ defines the momentum-space wave function. For axially deformed nuclei, the momentum wave function $\psi(\vec{k})$ can be expanded as:

$$\psi(\vec{k}) = \psi_{m_j}(\vec{k}) = \sum_{lj} \begin{pmatrix} f^{lj}(k)\phi_{ljm_j}(\Omega_k) \\ g^{lj}(k)\phi_{\tilde{l}jm_j}(\Omega_k) \end{pmatrix}, \tag{8}$$

with $\phi_{ljm_j}(\Omega_k) = \sum\limits_{m_s} \langle lm\frac{1}{2}m_s \,|jm_j\rangle Y_{lm}(\Omega_k)\chi_{m_s}$. Let χ_{m_s} denote the spin wave function and $Y_{lm}(\Omega_k)$ the spherical harmonics.

Application of Eq. (8) to Eq. (7) leads to a symmetric eigenvalue problem (see Ref. [40]). Solving this eigenvalue problem yields the energies of bound and resonant states on an equal footing. The wave functions are Fourier transformed into coordinate representation [40], with their upper and lower spinor components expressed as:

$$\begin{cases} G^{lj}(r)/r = -i^{l+1}\sqrt{\frac{2}{\pi}}\int k^2 dk j_l(kr) f^{lj}(k), \\ F^{lj}(r)/r = -i^{\tilde{l}}\sqrt{\frac{2}{\pi}}\int k^2 dk j_{\tilde{l}}(kr) g^{lj}(k). \end{cases} \tag{9}$$

In nuclei near the drip lines, the Fermi surface lies adjacent to the continuum threshold, enabling valence nucleons to readily populate unbound states. The BCS approach effectively captures pairings in this regime, with resonances accounted for in the revised gap equation.

$$\sum_b \frac{1}{\sqrt{\left(\varepsilon_b - \lambda\right)^2 + \Delta^2}} + \sum_r \int g_r(\varepsilon) \frac{1}{\sqrt{(\varepsilon - \lambda)^2 + \Delta^2}} d\varepsilon = \frac{2}{G}, \tag{10}$$

and the particle number equation

$$\sum_b \left(1 - \frac{\varepsilon_b - \lambda}{\sqrt{\left(\varepsilon_b - \lambda\right)^2 + \Delta^2}}\right) + \sum_r \int g_r(\varepsilon) \left(1 - \frac{\varepsilon - \lambda}{\sqrt{(\varepsilon - \lambda)^2 + \Delta^2}}\right) d\varepsilon = N. \tag{11}$$

For pairing strength G and particle number N, $g_r(\varepsilon)$ is given by: $g_r(\varepsilon) = \frac{1}{\pi}\frac{\Gamma_r/2}{(\varepsilon-\varepsilon_r)^2+\Gamma_r^2/4}$. Where ε_r and ε_b are the energy eigenvalues of H for resonant and bound states, respectively, and Γ_r quantifies the width of resonances. Occupation probabilities for both resonant and bound states are derived from Eqs. (10) and (11). Using the BCS approach to handle pairing, equations (10) and (11) are solved for G or Δ, where $\Delta = 12/\sqrt{A}$ approximates the neutron and proton gaps [65]. Occupation probabilities ν^2 are extracted from these solutions, while radial wave functions $F(r)$ and $G(r)$ are computed from Eq. (9), enabling the calculation of densities ρ_3, ρ_c, ρ_s and ρ_ν via Eqs. (5) and (6). These densities construct the sources in Eq. (3), which update the meson fields and potentials iteratively until stability.

III. NUMERICAL DETAILS AND RESULTS

To comprehensively investigate the structural evolution of neutron-rich magnesium isotopes, we employ the deformed relativistic mean-field theory in complex momentum representation with BCS pairing (DRMF-CMR-BCS). This sophisticated approach enables a unified description of bound states, resonant states, and the nonresonant continuum, which is crucial for accurately capturing the exotic phenomena emerging near the neutron drip line. The calculations are performed using the NL3 effective interaction [68], known for its reliable description of nuclear ground-state properties across the nuclear chart.

TABLE I. The quadruple deformation parameter β_2, two-neutron separation energy (S_{2n}), root-mean-square neutron radius (R_n) and root-mean-square matter radius (R_m) for even-even nuclei ^{34}Mg,^{36}Mg,^{38}Mg,^{40}Mg,^{42}Mg,^{44}Mg gained by the selfconsistent DRMF-CMR-BCS calculations with NL3. Experimental (Expt.) values of S_{2n} are taken from Refs [74].

Nuclei	β_2	S_{2n} [MeV]	Expt. S_{2n} [MeV]	R_n [fm]	R_m [fm]
^{34}Mg	0.320	6.816	6.990(29)	3.827	3.573
^{36}Mg	0.411	6.707	4.090(690)	4.118	3.809
^{38}Mg	0.296	2.729	2.450(850)	4.320	3.983
^{40}Mg	0.289	1.053	0.670(710)	4.440	4.097
^{42}Mg	0.360	-2.833		4.549	4.205
^{44}Mg	0.275	-1.615		6.057	5.424

The solution of the coupled Dirac and Klein-Gordon equations proceeds through an iterative self-consistent procedure. Initial parameterizations of the scalar and vector potentials $S(\vec{r})$ and $V(\vec{r})$ are constructed based on the expected nuclear density distributions. The transformation of the Dirac equation into the complex momentum representation, as given in Eq. (7), represents a cornerstone of our approach. This transformation allows for the direct computation of resonant states without imposing artificial boundary conditions, thereby providing access to the complete single-particle spectrum including narrow resonances that play pivotal roles in halo formation.

In the momentum-space formulation, the wave functions $f(k)$ and $g(k)$ are expanded in a coupled-channel basis characterized by angular momentum quantum numbers lj. The maximum momentum is set to $k_{\max} = 4.0$ fm^{-1}, sufficiently large to encompass all relevant momentum components contributing to both bound and continuum states.

A. Ground state properties

The ground state properties of ^{34,36,38,40,42,44}Mg are calculated using the self-consistent DRMF-CMR-BCS approach with NL3 in Table I, including quadruple deformation parameter β_2, two-neutron separation energies S_{2n}, root-mean-square (rms) neutron radii R_n and matter radii R_m. The two-neutron separation energies of ^{34}Mg, ^{36}Mg, ^{38}Mg, and ^{40}Mg are 6.990 MeV, 4.090 MeV, 2.450 MeV and 1.870 MeV in AME2016 [69–71] respectively. The empirical value of S_{2n} of ^{40}Mg is 0.670 MeV in AME2020 [72–74], while others are consistent with AME2016 data. Experimental data for the two-neutron separation energies of ^{42,44}Mg have not yet been available to date. In Table I, the calculated S_{2n} of ^{34,36}Mg is 6.816 MeV and 6.707 MeV. ^{38}Mg is bound with NL3 (S_{2n} =2.729 MeV). The calculated S_{2n} for ^{40}Mg is 1.053 MeV. The calculated S_{2n} of ^{42}Mg is -2.833 MeV. ^{44}Mg is bound (S_{2n} =-1.615 MeV). These results indicate that the two-neutron drip line nucleus of the Mg isotopes is ^{40}Mg.

It should be noted that the NL3 interaction tends to overbind neutron-rich nuclei in magnesium isotopes. This is reflected in the calculated S_{2n} values for ^{36}Mg and ^{40}Mg, which are larger than the experimental data. This overbinding is a known limitation of the NL3 parameter set [68]. Nevertheless, the systematic trend of decreasing S_{2n} with increasing neutron number is reproduced, and the main conclusions regarding shell evolution and halo formation in the heavier isotopes ^{40,42,44}Mg are robust against this limitation, as further supported by calculations with the PK1 interaction.

In Table I, the calculated ground-state β_2 values are all positive, indicating prolate deformation for all isotopes. These values are 0.320, 0.411, 0.296, 0.289, 0.360, and 0.275 for ^{34}Mg, ^{36}Mg, ^{38}Mg, ^{40}Mg, ^{42}Mg, and ^{44}Mg, respectively. The deformation shows a non-monotonic trend with neutron number, reflecting the complex interplay between shell structure and deformation.

The nuclear radius is an important observable that reflects the spatial extension of the nuclear density. As shown in the Table I, the calculated matter and neutron rms radii increase with neutron number. Notably, the neutron radius of ^{44}Mg is significantly larger than those of its neighboring isotopes, suggesting the emergence of a neutron halo structure, consistent with the result in Ref. [40].

B. Complex momentum contour and resonance treatment

The proper treatment of resonant states necessitates careful definition of the integration contour in the complex momentum contour. Following the methodology established in Ref. [41], we construct a piecewise contour connecting four characteristic points, denoted as k_1, k_2, k_3, and $k_{\max}$. This contour selection is physically motivated by the need to enclose those narrow resonances that significantly contribute to the Berggren completeness relation. The imaginary components of k_2 are carefully chosen to capture the decay widths of specific resonant states while avoiding numerical instabilities. The robustness of our results with respect to contour variations has been verified, ensuring that the physical conclusions are not artifacts of the computational methodology.

For narrow resonances, the CMR method directly solves the eigenvalue problem along a properly chosen complex momentum contour that encloses these states. For broad resonances, which are more difficult to capture with a single contour, we employ the complex momentum representation combined with Green's function method [38] to compute the continuum level density. The resonance parameters are then extracted from the peaks in the continuum level density, a procedure that remains numerically stable even for broad resonances.

C. Single-particle structure and shell evolution mechanisms

Fig. 1 presents a comprehensive overview of the single-neutron spectra for even-even nuclei $^{34-44}$Mg, revealing profound insights into the shell evolution of neutron-rich nuclei. The systematic lowering of certain orbitals drives the disappearance of traditional magic numbers, a phenomenon that can be understood through multiple competing mechanisms.

The collapse of the $N = 20$ shell closure is primarily attributable to the downward shift of the $1/2_1^-$ orbital, which originates from the $2p_{1/2}$ shell. This shift results from the reduced neutron-proton interaction strength in extremely neutron-rich nuclei, leading to a weakening of the spin-orbit potential that normally stabilizes shell closures. In addition, the monopole drift of the neutron $1d_{3/2}$ and $2p_{3/2}$ orbitals, driven by the gradual depletion of protons in the $1d_{5/2}$ orbital, further reduces the $N = 20$ shell gap. The stabilization of prolate de-

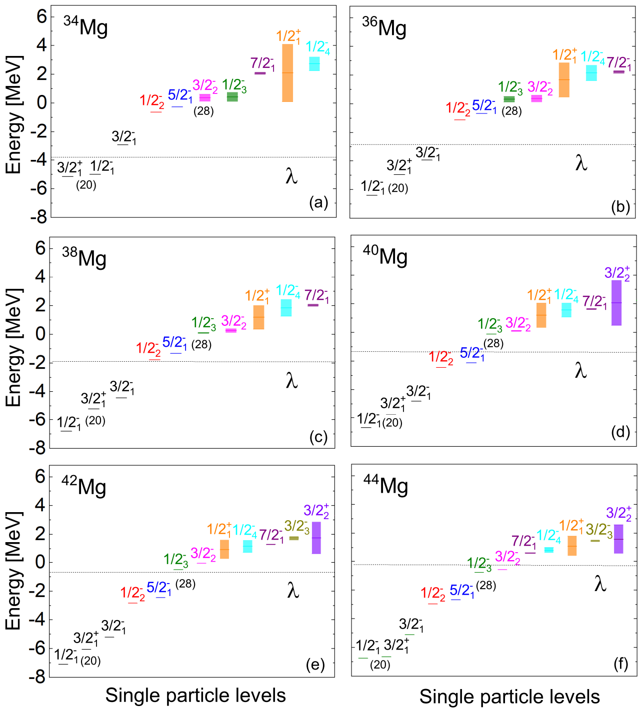

FIG. 1. (color online) Single-neutron spectra for even-even nuclei $^{34-44}$Mg, showing bound states (solid lines) and resonances (error bars). The systematic downward shift of key orbitals drives shell closure collapse through monopole drift and configuration mixing.

formation in these isotopes also contributes to the shell quenching by mixing orbitals from different harmonic oscillator shells, leading to enhanced configuration mixing and a reduced level spacing near the Fermi surface. The calculated deformation parameters β_2 presented in Table I confirm the prolate shapes across the isotopic chain, supporting the role of deformation in the shell evolution.

Simultaneously, the $N = 28$ shell closure disappears in ^{34,36}Mg due to the concerted lowering of the $1/2^-_3$ and $3/2^-_2$ orbitals. These states derive from the $2p_{3/2}$ and $1f_{7/2}$ shells, respectively. The reduction of the $N = 28$ gap can be understood through the monopole drift of the neutron $1f_{7/2}$ orbital as protons are depleted from the $1d_{5/2}$ orbital, combined with the weakening of the spin-orbit splitting in neutron-rich nuclei. Furthermore, the emergence of stable prolate deformation in these isotopes amplifies the shell collapse by mixing orbitals from different harmonic oscillator shells, leading to enhanced configuration mixing and a reduced level spacing near the Fermi surface. As shown in Table I, all isotopes from ^{34}Mg to ^{44}Mg exhibit prolate deformation, with β_2 values reaching up to 0.411 for ^{36}Mg, which supports the role of deformation in the shell evolution.

The resonant states exhibit a remarkable diversity in their widths, reflecting their different coupling strengths to the continuum. Broad resonances such as the $1/2^+_1$ state across all isotopes, the $1/2^-_4$ state in ^{38}Mg, and the $3/2^+_2$ states in ^{40,42,44}Mg indicate strong coupling to the non-resonant continuum and short lifetimes. These states typically have wavefunctions with significant amplitude in the classically forbidden region, facilitating rapid decay. In contrast, narrow resonances such as $3/2^-_2$ in ^{40}Mg and $7/2^-_1$ in ^{42}Mg retain quasi-bound character due to centrifugal barriers or specific nodal structures that suppress their decay amplitudes.

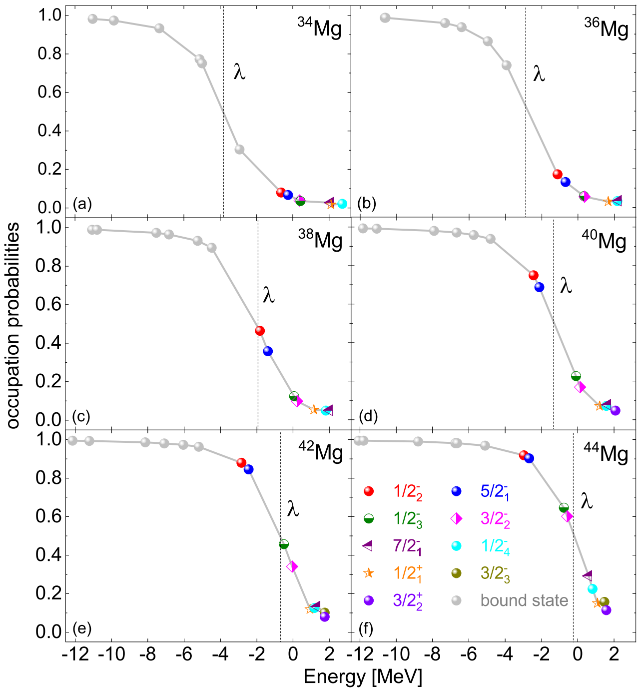

FIG. 2. (color online) Occupation probabilities near the Fermi surface. Anomalous occupancies of narrow resonances highlight their role in stabilizing exotic configurations through pairing-enhanced continuum coupling.

D. Occupation patterns and pairing correlations

Fig. 2 displays the occupation probabilities of single-particle orbitals near the Fermi surface, revealing intriguing patterns that deviate from simple Fermi-Dirac statistics. While the general trend shows decreasing occupancy with increasing energy, several notable anomalies emerge that provide insights into the pairing correlations and structural evolution.

The anomalous behavior of the $1/2^-_4$ orbitals in ^{34,36,40,42}Mg and the $3/2^-_3$ orbital in ^{44}Mg, and the $3/2^-_3$ orbital in ^{44}Mg, exhibiting higher energies yet larger occupation probabilities than their neighboring $1/2^+_1$ states, can be understood through the interplay between single-particle energies and pairing correlations. The BCS formalism, as implemented in our approach, allows nucleon pairs to scatter into states above the Fermi energy if those states have favorable properties such as narrow widths and appropriate quantum numbers for pairing. The enhanced occupancy of narrow resonances underscores their role in stabilizing exotic configurations

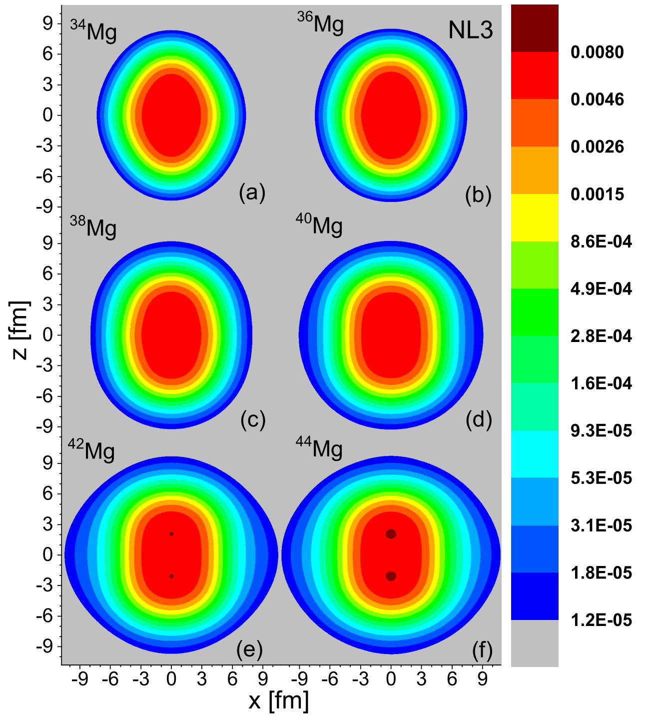

FIG. 3. (color online) Two-dimensional neutron density distributions showing the evolution from compact to diffuse structures in even-even nuclei $^{34-44}$Mg, with clear evidence of surface deformation and halo formation.

through pairing correlations, which preferentially scatter nucleon pairs into long-lived resonant states near the Fermi surface.

Similarly, the systematic elevation of $7/2^-_1$ orbital occupancies in ^{36,38,40,42}Mg relative to nearby $1/2^-_4$ states reflects the sensitivity of pairing to the detailed structure of the single-particle spectrum. The $7/2^-_1$ orbitals, despite their higher energies, benefit from their narrow widths and specific angular momentum coupling schemes that enhance their pairing matrix elements.

These occupation anomalies are not merely curiosities, they have profound implications for nuclear stability and structure. The partial occupation of resonant states above the Fermi energy provides additional binding through pairing correlations, potentially stabilizing nuclei that would otherwise be unbound. Furthermore, these occupation patterns directly influence the density distributions and deformation properties, as discussed in subsequent sections.

E. Neutron density distributions and the emergence of halo structures

The two-dimensional neutron density distributions for even-even nuclei $^{34-44}$Mg, presented in Fig. 3, reveal a systematic evolution from compact structures to diffuse halo systems. A clear trend of increasing spatial extension with neutron number is observed, particularly for ^{40,42,44}Mg, which exhibit pronounced diffuse tails characteristic of halo formation.

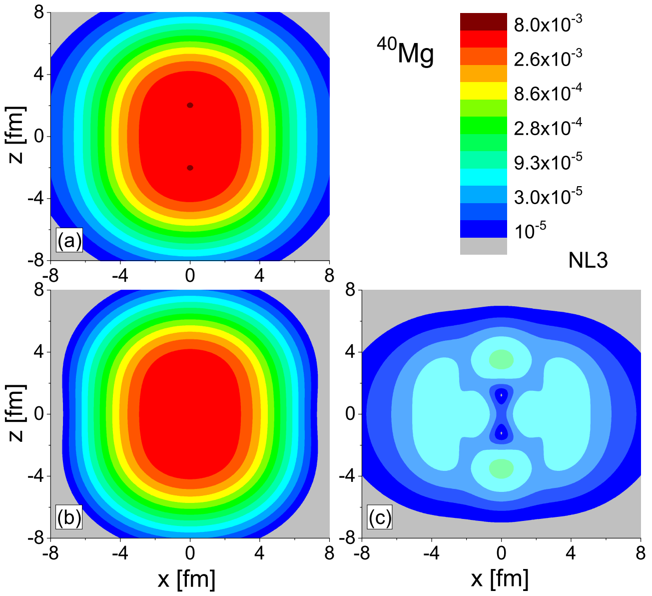

FIG. 4. (color online) Neutron density distributions in ^{40}Mg obtained with the NL3 interaction: (a) total, (b) core, (c) halo. The prolate core and oblate halo illustrate the shape decoupling phenomenon.

The transition to halo structures can be understood through the decreasing single-particle energies near the Fermi surface and the increasing role of the continuum. As neutrons are added, the Fermi energy approaches the particle emission threshold, causing the valence neutrons to occupy increasingly diffuse orbitals. The most pronounced halo signatures are seen in ^{40}Mg, ^{42}Mg, and ^{44}Mg, whose density profiles extend far beyond the core region, forming what can be characterized as "skin" or "halo" structures depending on the specific orbital compositions.

To elucidate the microscopic origin of these halo structures, we decompose the total neutron density into core and halo components based on the energy gaps evident in the single-particle spectra in Fig. 1. The core consists of deeply bound orbitals that maintain a compact spatial distribution, while the halo comprises weakly bound and resonant orbitals near the Fermi surface that contribute to the diffuse tail.

1. *Halo structure and shape decoupling in ^{40}Mg*

Fig. 4(a) shows the total neutron density of ^{40}Mg, which exhibits a markedly diffuse spatial distribution extending significantly beyond the core region. The core density (Fig. 4(b)) is compact and exhibits a prolate deformation, reflecting the alignment of high-Ω orbitals along the symmetry axis. In striking contrast, the halo density (Fig. 4(c)) is extended and displays an oblate

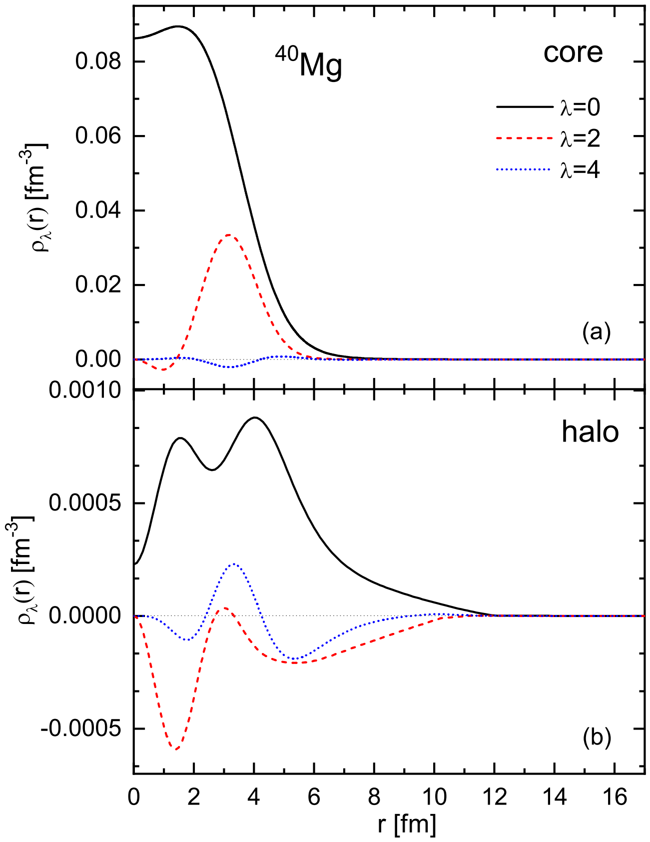

FIG. 5. (color online) Multipole decomposition of neutron densities in ^{40}Mg: (a) core, (b) halo. The positive quadrupole moment of the core and negative moment of the halo provide quantitative evidence for shape decoupling.

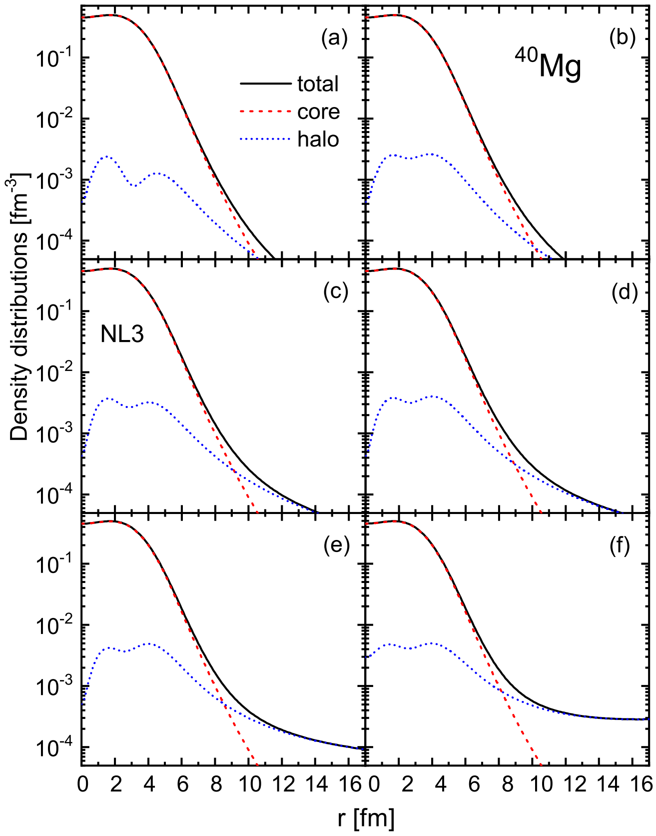

FIG. 6. (color online) The figure displays the total neutron density distributions (black solid line), neutron core density distributions (red dash-dot line), and neutron halo density distributions (blue short dot line) in ^{40}Mg. The various subfigures present the neutron halo density distributions corresponding to different numbers of occupied resonant levels.

deformation, a clear manifestation of shape decoupling between core and halo.

This decoupling phenomenon is quantitatively analyzed in Fig. 5 through multipole decomposition of the density distributions. The core component shows a positive quadrupole moment ($\lambda = 2$) consistent with prolate deformation, while the halo exhibits a negative quadrupole moment indicating oblate deformation. Additionally, a significant hexadecapole moment ($\lambda = 4$) is present in the halo, revealing complex deformation beyond the simple quadrupole shape. This multipole structure arises from the specific angular momentum composition of the halo-forming orbitals and their spatial distributions.

To clarify how weakly bound and resonant states drive neutron halo formation, the total neutron density distribution, the neutron core and neutron halo density distribution are presented in Fig. 6 for the neutron-rich nuclei ^{40}Mg. We separate the total neutron density distribution into core and halo parts following the energy gap shown in Fig. 1, with a demarcation boundary between the orbitals $5/2_1^-$ and $1/2_3^-$. The deeply bound orbital $5/2_1^-$ and lower-lying orbitals contribute to the tight neutron core density, while the weakly bound orbital $1/2_3^-$ and higher-lying unbound orbitals collectively form the spatially extended neutron halo part. In each panel of Fig. 6, the orbitals that constitute the neutron core of ^{40}Mg are the same, but those that form the neutron halo are different.

For ^{40}Mg, the neutron halo density in Fig. 6(a) originates solely from the weakly bound orbital $1/2_3^-$, which exhibits limited spatial diffuseness and thus provides a negligible contribution to the halo structure. The total neutron density and halo density distributions are systematically demonstrated in Fig. 6(a)-(f), progressively incorporating resonant orbitals ordered by their proximity to the real momentum axis (from nearest to farthest). In Fig. 6(b), the halo density includes contributions from both the weakly bound orbital $1/2_3^-$ and the resonant orbital $7/2_1^-$. Fig. 6(c) illustrates contributions from the orbital $1/2_3^-$ combined with two resonant orbitals $7/2_1^-$ and $3/2_2^-$. Fig. 6(d) displays contributions from the orbital $1/2_3^-$ and three resonant orbitals $7/2_1^-$, $3/2_2^-$, and $3/2_2^+$. Fig. 6(e) incorporates the orbital $1/2_3^-$ with four resonant orbitals $7/2_1^-$, $3/2_2^-$, $3/2_2^+$ and $1/2_4^-$, while Fig. 6(f) exhibits the neutron halo density composed of

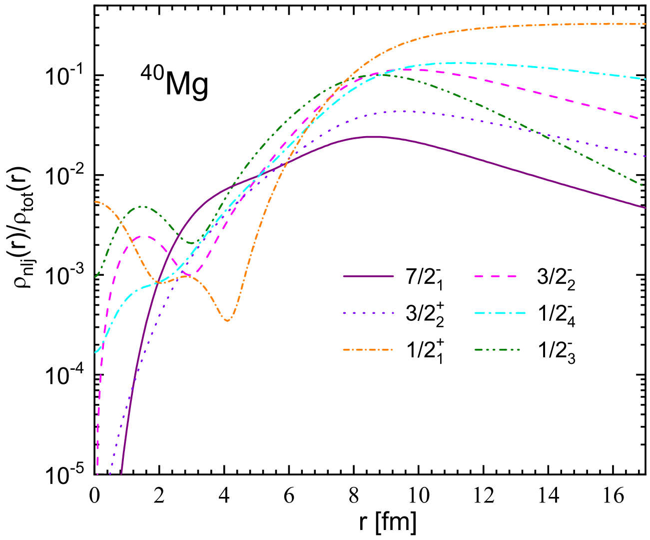

FIG. 7. (color online) Ratios of orbital neutron densities to the total density in ^{40}Mg. The $3/2_2^-$ resonance dominates the halo contribution, while centrifugal suppression limits the role of high-l orbitals.

the orbital $1/2_3^-$ and five resonant orbitals $7/2_1^-$, $3/2_2^-$, $3/2_2^+$, $1/2_4^-$, and $1/2_1^+$. As the number of resonant orbitals increases in Fig. 6, both the total neutron density and halo density distributions exhibit enhanced spatial diffuseness. Remarkably, the inclusion of the resonant orbitals $1/2_4^-$ and $1/2_1^+$ drives considerable modifications to the density profiles, as seen in the transitions from Fig. 6(d) to 6(e) and subsequently to 6(f). These findings highlight the pivotal role of resonant orbitals, particularly those farther from the real momentum axis, in shaping the halo structure of weakly bound nuclei.

To identify the specific orbitals responsible for the halo formation, Fig. 7 shows the ratios of the neutron density distributions of weakly bound and resonant orbitals compared to the total neutron densityfor ^{40}Mg. The analysis reveals that the halo in ^{40}Mg is dominated by the narrow resonance $3/2_2^-$, which possesses a large spatial extent and a significant occupation probability of 0.1688. As quantitatively shown in Fig. 7, this orbital contributes the most to the halo density due to its dominant character $2p_{3/2}$ (91.7%) and the absence of a strong centrifugal barrier. The weakly bound orbital $1/2_3^-$ also contributes, though less significantly, due to its mixed $2p_{3/2}$ and $2p_{1/2}$ composition. In contrast, broad resonances such as $1/2_1^+$ and $3/2_2^+$ exhibit diffuse densities but make limited contributions to the halo due to their low occupation probabilities (0.0696 and 0.0576, respectively). High orbital angular momentum states such as $7/2_1^-$ and $1/2_4^-$ are spatially constrained by centrifugal barriers, despite their narrow widths and appreciable occupancies in some cases. In the present calculation, the neutron number occupying these orbitals that contribute to the halo is approximately equal to 1.3, which is the cause of the exotic halo phenomenon in ^{40}Mg.

The emergence of an oblate halo in ^{40}Mg arises fundamentally from the occupancy of orbitals with low projection quantum numbers Ω and significant p-wave components. These orbitals favor surface localization in directions perpendicular to the symmetry axis, leading to an oblate density distribution. This contrasts with the prolate core, whose density is shaped by high-Ω orbitals aligned along the symmetry axis. The resulting shape decoupling represents a characteristic of halo nuclei near the drip line, where the competition between continuum coupling, deformation, and pairing correlations determines the ground state morphology.

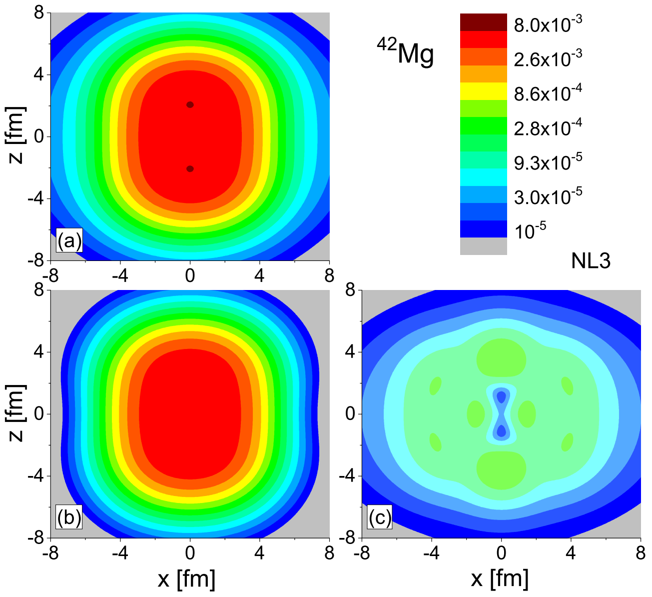

FIG. 8. (color online) Neutron density distributions in ^{42}Mg obtained with the NL3 interaction: (a) total, (b) core, (c) halo. The enhanced diffuseness compared to ^{40}Mg reflects the stronger halo development in this isotope.

2. *Halo structure and shape decoupling in ^{42}Mg*

The total neutron density of ^{42}Mg (Fig. 8(a)) exhibits even greater diffusivity than that of ^{40}Mg, reflecting the increased neutron excess and stronger continuum coupling. The core density (Fig. 8(b)) maintains a prolate shape, while the halo density (Fig. 8(c)) again displays an oblate deformation, confirming the persistence of shape decoupling in this more neutron-rich isotope.

The multipole decomposition in Fig. 9 provides quantitative support for this interpretation, showing a positive quadrupole moment for the core and a negative one for the halo. Non-negligible hexadecapole moments are again present, indicating that the deformation can not be fully described by quadrupole moments alone.

To elucidate the mechanism by which weakly bound and resonant states govern neutron halo formation,

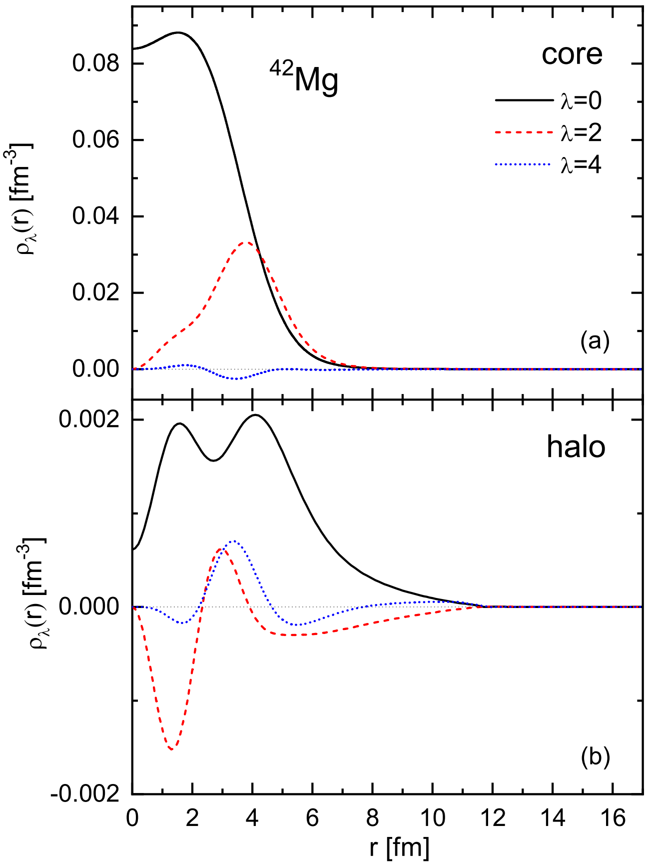

FIG. 9. (color online) Multipole decomposition of neutron densities in ^{42}Mg: (a) core, (b) halo.

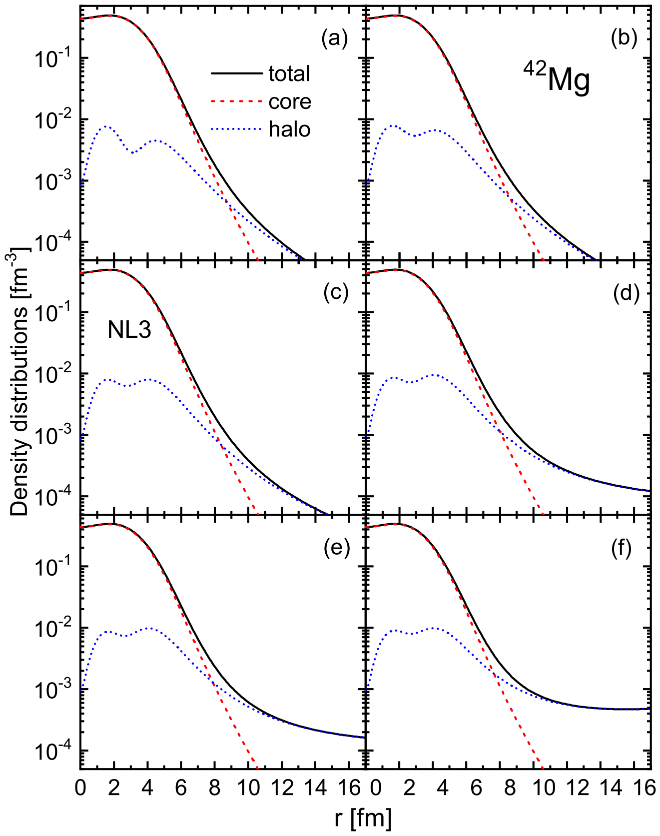

FIG. 10. (color online) The figure displays the total neutron density distributions (black solid line), neutron core density distributions (red dash-dot line), and neutron halo density distributions (blue short dot line) in ^{42}Mg. The various subfigures present the neutron halo density distributions corresponding to different numbers of occupied resonant levels.

Fig. 10 shows the total neutron density distribution, the core and halo density distribution for the neutron-rich nucleus ^{42}Mg. The total neutron density distribution is decomposed into core and halo components based on the big energy gap illustrated in Fig. 1, with the orbital boundary defined between the orbitals $5/2_1^-$ and $1/2_3^-$. The compact core density arises from the orbital $5/2_1^-$ and lower-lying orbitals, whereas the diffuse halo component emerges from the weakly bound orbital $1/2_3^-$ and higher-lying unbound orbitals.

For ^{42}Mg, the neutron halo density distribution is displayed in Fig. 10(a), which comprises contributions from two weakly bound orbitals $3/2_2^-$ and $1/2_3^-$. These weakly bound orbitals demonstrate relatively dense spatial allocation, showing their limited contribution to the extended halo structure. The evolution of the total neutron density and halo density distributions is exhaustively illustrated in Fig. 10(a)-(f), where resonant states are progressively included based on their distance from the real momentum axis. The halo density depicted in Fig. 10(b) consists of two weakly bound orbitals $3/2_2^-$ and $1/2_3^-$, and one resonant orbital $7/2_1^-$. Subsequent subfigures reveal the incremental addition of resonant orbitals: two resonant orbitals $7/2_1^-$ and $3/2_3^-$ in Fig. 10(c), three resonant orbitals $7/2_1^-$, $3/2_3^-$ and $1/2_4^-$ in Fig. 10(d), four resonant orbitals $7/2_1^-$, $3/2_3^-$, $1/2_4^-$ and $1/2_1^+$ in Fig. 10(e), and five resonant orbitals $7/2_1^-$, $3/2_3^-$, $1/2_4^-$, $1/2_1^+$ and $3/2_2^+$ in Fig. 10(f). A clear trend emerges: the incorporation of additional resonant orbitals leads to a progressive decentralization of both the total neutron density and halo density distributions. Among them, the resonant orbitals $1/2_1^+$ and $3/2_2^+$ substantially contribute to the total neutron density and the neutron halo density [transitioning from Fig. 10 (d) to Fig. 10 (e), and from Fig. 10 (e) to Fig. 10 (f)].

To quantitatively assess the contributions of weakly bound and resonant orbitals to the neutron halo formation in ^{42}Mg, the ratios of the neutron density distributions of weakly bound and resonant orbitals compared to the total neutron density are presented in Fig. 11 for ^{42}Mg. Subsequent analysis of these distribution ratios reveals signatures of a potential exotic halo structure in this neutron-rich isotope. In contrast to ^{40}Mg, the halo in ^{42}Mg is primarily formed by the weakly bound orbital $3/2_2^-$, which possesses a high occupancy (0.3417) and a diffuse density dominated by the shell $2p_{3/2}$ (90.7%). The orbital $1/2_3^-$ also contributes significantly due to its high occupancy (0.4565) and mixed character $2p_{3/2}$-

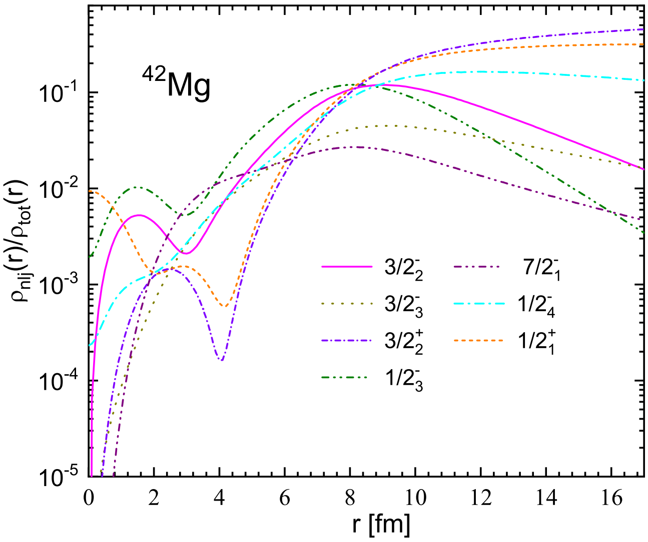

FIG. 11. (color online) Orbital density ratios in ^{42}Mg. The weakly bound $3/2^-_2$ orbital is the dominant halo contributor, with significant support from the $1/2^-_3$ orbital.

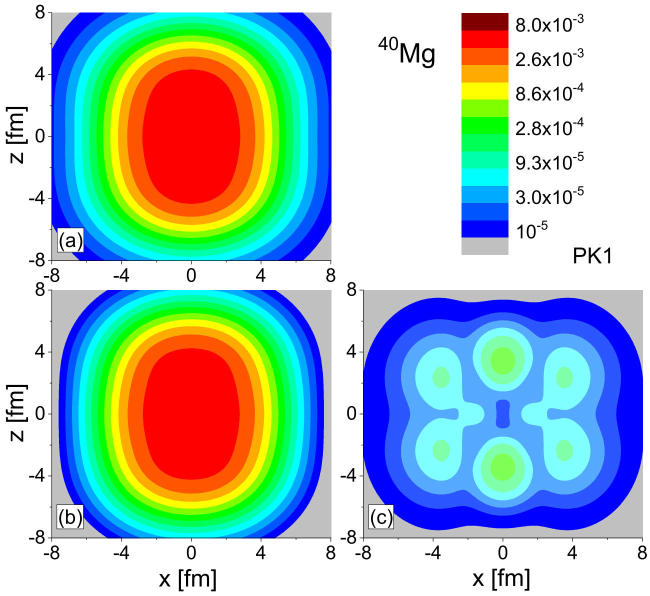

FIG. 12. (color online) Same as Fig. 4 but obtained with the PK1 effective interaction [75]. Neutron density distributions in ^{40}Mg: (a) total, (b) core, (c) halo. The prolate core and oblate halo remain clearly visible, confirming the shape decoupling phenomenon.

$2p_{1/2}$-$1f_{5/2}$. Resonant orbitals such as $1/2^+_1$ and $3/2^+_2$ are spatially extended but have low occupation probabilities and experience strong centrifugal barriers, limiting their contributions to the halo. In the present calculation, the neutron number occupying these orbitals that contribute to the halo is approximately equal to 2.7, which is the cause of the exotic halo phenomenon in ^{42}Mg.

Although the orbitals such as $1/2^+_1$ exhibit remarkable spatial extension in the incremental construction process

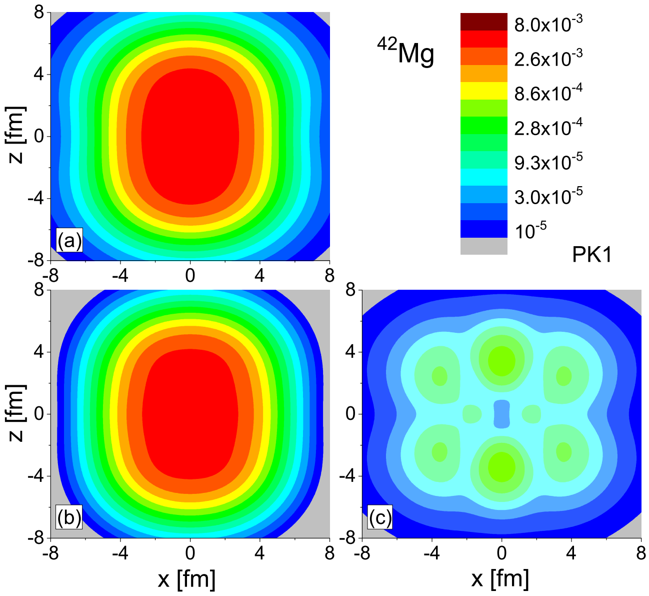

FIG. 13. (color online) Same as Fig. 8 but obtained with the PK1 effective interaction [75]. Neutron density distributions in ^{42}Mg: (a) total, (b) core, (c) halo. The enhanced diffuseness compared to ^{40}Mg and the oblate halo shape are again observed, consistent with the PK1 results.

(Figs. 6 and 10), their actual quantitative contribution to the total halo remains limited (Figs. 7 and 11). This is because halo formation depends not only on the spatial diffuseness of the orbitals but, more critically, on their occupation probabilities. Broadly resonant states for ^{40,42}Mg like $1/2^+_1$, with relatively low occupation probabilities, predominantly serve as "shape formers" for the halo, whereas narrow resonant state for ^{40}Mg or weakly bound state for ^{42}Mg such as $3/2^-_2$, characterized by high occupation probabilities, act as the primary "matter providers" for the halo.

The halo in ^{42}Mg is more diffuse than in ^{40}Mg, consistent with its larger RMS neutron radius. This increased diffusivity stems from the higher occupancy of the $3/2^-_2$ orbital and the greater number of neutrons in the halo region. The persistence of shape decoupling across both isotopes highlights a universal mechanism in which the halo forms from low-Ω, low-l orbitals that decouple from the prolate core due to their spatial extension and anisotropic occupancy.

3. *Results with the PK1 interaction*

To assess the dependence of our conclusions on the choice of effective interaction, we have repeated the calculations for the key isotopes ^{40}Mg and ^{42}Mg using the PK1 parameter set [75]. The resulting total neutron density distributions are shown in Figs. 12 and 13, respectively. As seen in Fig. 12, the PK1 calculation for ^{40}Mg also exhibits a prolate core and an oblate halo, fully consistent with the shape decoupling phenomenon observed with NL3 in Fig. 4. The halo of ^{42}Mg in Fig. 13 again shows more diffuse than in ^{40}Mg, and the oblate shape of the halo remains evident. These results indicate that the predicted shape decoupling and the isotopic dependence of halo development are robust features, not artifacts of the NL3 parametrization.

F. Orbital contributions and centrifugal barrier effects

The quantitative analysis of orbital contributions to the halo, as presented in Figs. 7 and 11, reveals the critical role of centrifugal barriers in suppressing halo formation from high-angular-momentum orbitals. For both ^{40}Mg and ^{42}Mg, orbitals with $l \geq 2$ exhibit significantly reduced halo contributions despite potentially favorable other properties.

In ^{40}Mg, the $7/2_1^-$ orbital ($l = 3$) displays minimal halo contribution due to the strong $l(l+1)/r^2$ centrifugal barrier that confines the wavefunction to the nuclear interior. Similarly, in ^{42}Mg, the $3/2_3^-$ and $1/2_4^-$ orbitals, despite their diffuse character, are hindered by their dominant f-wave components ($l = 3$). This suppression mechanism explains why halo formation preferentially occurs through s- and p-wave orbitals, which experience no or minimal centrifugal barriers.

The occupation probabilities further modulate these contributions. Even spatially diffuse orbitals with low angular momentum can not significantly contribute to the halo if their occupation probabilities are low, as is the case for the resonances $1/2_1^+$ and $3/2_2^+$ in both isotopes. This interplay between spatial extension, centrifugal barriers, and occupation probability creates a complex landscape for halo formation that is sensitively dependent on the detailed single-particle structure near the Fermi surface.

G. Systematic structural evolution and implications

The comprehensive analysis of even-even nuclei $^{34-44}$Mg reveals a consistent picture of shell quenching, deformation, and halo formation driven by the interplay of multiple nuclear structure effects. The collapse of the $N = 20$ and $N = 28$ magic numbers results from the combined action of reduced spin-orbit splittings, monopole drift of key neutron orbitals, and the on-set of stable prolate deformation. Halo structures emerge in ^{40,42,44}Mg, characterized by spatially extended neutron densities and shape decoupling between prolate cores and oblate halos.

This systematic evolution demonstrates how the delicate balance between single-particle energies, pairing correlations, and continuum coupling determines the structure of neutron-rich nuclei. The halo is primarily formed by weakly bound or narrow resonant orbitals with low angular momentum, such as $3/2_2^-$ and $1/2_3^-$, while high-l orbitals are suppressed by centrifugal barriers despite their potentially favorable other properties.

The DRMF-CMR-BCS approach provides a unified description of these effects, revealing how the complex interplay between single-particle structure, pairing, and continuum coupling gives rise to the exotic phenomena observed near the neutron drip line. These findings not only elucidate the specific case of magnesium isotopes but also provide broader insights into the structural evolution of neutron-rich nuclei across the nuclear landscape.

IV. SUMMARY

We have presented a systematic investigation of the neutron-rich magnesium isotopes $^{34-44}$Mg using the DRMF-CMR-BCS framework, which self-consistently unifies deformation, pairing, and continuum coupling. Our calculations reveal the microscopic mechanism behind the collapse of the $N = 20$ and $N = 28$ shell closures, identifying it as a cooperation of monopole drift in key neutron orbitals (e.g., $1/2_1^-$, $3/2_2^-$) and the stabilization of prolate deformation. The calculated deformation parameters, summarized in Table I, show consistently prolate shapes across the isotopic chain, supporting the role of deformation in the shell evolution.

A key finding is the universal emergence of deformed halos in ^{40,42,44}Mg, characterized by a striking shape decoupling: a prolate core coexists with an oblate halo. Multipole decomposition confirms this decoupling arises from the distinct spatial distributions of core and halo nucleons. The halo is predominantly formed by low-angular-momentum orbitals (s- and p-waves) near the Fermi surface, while high-l orbitals are suppressed by centrifugal barriers.

Notably, the halo formation mechanism exhibits an isotopic dependence: in ^{40}Mg, the narrow resonant state $3/2_2^-$ is dominant, whereas in ^{42}Mg, the weakly bound orbital $3/2_2^-$ plays the primary role, with the $1/2_3^-$ orbital contributing significantly in both cases. The anomalous occupancy of narrow resonances underscores the important role of pairing enhanced continuum coupling in stabilizing these exotic structures.

In conclusion, the structure of neutron-rich Mg isotopes is governed by the intricate competition between single-particle energies, deformation, pairing, and the continuum. In contrast to our previous work [40] which focused on a single isotope, the present systematic study establishes shape decoupling as a universal phenomenon in neutron-rich magnesium isotopes and reveals the isotopic dependence of halo formation mechanisms, and offers clear testable predictions for future rare-isotope beam experiments through observables like reaction cross-sections and Coulomb excitation.

ACKNOWLEDGMENTS

This work was supported by the National Natural Science Foundation of China (Grants No. 12475116, No. 12475115, No. 11935001 and No. 12305084), the Talent Research Funding Project of Hefei Institute of Technology (Program No. 2025KY06, No. 2025KY49), the Scientific Research Project of Anhui Provincial Department of Education(Program No. 2025AHGXZK40204), and partially by the Anhui Provincial Quality Engineering Project for Higher Education Institutions (Program No. 2024syyj047).

[1] E. Leistenschneider, E. Dunling, and G. Bollen et al., Precision mass measurements of neutron-rich scandium isotopes refine the evolution of $N = 32$ and $N = 34$ shell closures. Phys. Rev. Lett. **126**, 042501 (2021). doi:10.1103/PhysRevLett.126.042501

[2] X. F. Yang, C. Wraith, and L. Xie et al., Isomer shift and magnetic moment of the long-lived $1/2^+$ isomer in $^{79}_{30}Zn^{49}$: signature of shape coexistence near ^{78}Ni. Phys. Rev. Lett. **116**, 182502 (2016). doi:10.1103/PhysRevLett.116.219901

[3] T. Otsuka, and Y. Tsunoda, The role of shell evolution in shape coexistence. J. Phys. G: Nucl. Part. Phys. **43**, 024009 (2016). doi:10.1088/0954-3899/43/2/024009

[4] H. Nishibata, S. Kanaya, and T. Shimoda et al., Structure of Mg^{31}: Shape coexistence revealed by β-γ spectroscopy with spin-polarized Na^{31}. Phys. Rev. C **99**, 024322 (2019). doi:10.1103/PhysRevC.99.024322

[5] G. L. Wilson, W. N. Catford, and N. A. Orr et al., Shell evolution approaching the $N = 20$ island of inversion: structure of ^{26}Na. Phys. Lett. B **759**, 417 (2016). doi:10.1016/j.physletb.2016.05.093

[6] B. Longfellow, D. Weisshaar, and A. Gade et al., Shape Changes in the $N = 28$ Island of Inversion: Collective Structures Built on Configuration-Coexisting States in S^{4}3. Phys. Rev. Lett. **125**, 232501 (2020). doi:10.1103/PhysRevLett.125.232501

[7] J. Meng, and P. Ring, Relativistic Hartree-Bogoliubov Description of the Neutron Halo in ^{11}Li. Phys. Rev. Lett. **77**, 3963 (1996). doi:10.1103/PhysRevLett.77.3963

[8] S. Bagchi, R. Kanungo, and Y. K. Tanaka et al., Two-Neutron Halo is Unveiled in ^{29}F. Phys. Rev. Lett. **124**, 222504 (2020). doi:10.1103/PhysRevLett.124.222504

[9] J. Meng, H. Toki, and S. G. Zhou et al., Relativistic Continuum Hartree Bogoliubov theory for ground state properties of exotic nuclei. Prog. Part. Nucl. Phys. **57**, 470 (2006). doi:10.1016/j.ppnp.2005.06.001

[10] J. Meng, and S. G. Zhou, Halos in medium-heavy and heavy nuclei with covariant density functional theory in continuum. J. Phys. G: Nucl. Part. Phys. **42**, 093101 (2015). doi:10.1088/0954-3899/42/9/093101

[11] E. P. Wigner, and L. Eisenbud, Higher Angular Momenta and Long Range Interaction in Resonance Reactions. Phys. Rev. **72**, 29 (1947). doi:10.1103/PhysRev.72.29

[12] G. M. Hale, R. E. Brown, and N. Jarmie, Pole structure of the $J^{\Pi} = 3/2^+$ resonance in ^{5}He. Phys. Rev. Lett. **59**, 763 (1987). doi:10.1103/PhysRevLett.59.763

[13] J. Humblet, B. W. Filippone, and S. E. Koonin, Level matrix, ^{16}N β decay, and the ^{12}C(α,γ) ^{16}O reaction. Phys. Rev. C **44**, 2530 (1991). doi:10.1103/PhysRevC.44.2530

[14] V. I. Kukulin, V. M. Krasnopl'sky, and J. Horácek, *Theory of Resonances: Principles and Applications* (Kluwer Academic, Dordrecht, 1989).

[15] E. N. Economou, *Green's Functions in Quantum Physics* (Springer-Verlag, Berlin, 2006).

[16] Y. Zhang, M. Matsuo, and J. Meng, Pair correlation of giant halo nuclei in continuum Skyrme-Hartree-Fock-Bogoliubov theory. Phys. Rev. C **86**, 054318 (2012). doi:10.1103/PhysRevC.86.054318

[17] T. T. Sun, S. Q. Zhang, and Y. Zhang et al., Green's function method for single-particle resonant states in relativistic mean field theory. Phys. Rev. C **90**, 054321 (2014). doi:10.1103/PhysRevC.90.054321

[18] J. R. Taylor, *Scattering Theory: The Quantum Theory on Nonrelativistic Collisions* (John Wiley & Sons, New York, 1972).

[19] Z. P. Li, J. Meng, and Y. Zhang et al., Single-particle resonances in a deformed Dirac equation. Phys. Rev. C **81**, 034311 (2010). doi:10.1103/PhysRevC.81.034311

[20] Z. P. Li, Y. Zhang, and D. Vretenar et al., Single-particle resonances in a deformed relativistic potential. Sci. China Phys. Mech. Astron. **53**, 773 (2010). doi:/10.1007/s11433-010-0161-7

[21] N. Moiseyev, Quantum theory of resonances: calculating energies, widths and cross-sections by complex scaling. Phys. Rep. **302**, 212 (1998). doi:10.1016/S0370-1573(98)00002-7

[22] P. Navrátil, and W. E. Ormand, Ab Initio Shell Model Calculations with Three-Body Effective Interactions for p-Shell Nuclei. Phys. Rev. Lett. **88**, 152502 (2002). doi:10.1103/PhysRevLett.88.152502

[23] S. C. Pieper, and R. B. Wiringa, Quantum Monte Carlo calculations of light nuclei. Ann. Rev. Nucl. Part. Sci. **51**, 53 (2001). doi:10.1146/annurev.nucl.51.101701.132506

[24] D. J. Dean, and M. Hjorth-Jensen, Pairing in nuclear systems: From neutron stars to finite nuclei. Rev. Mod. Phys. **75**, 607 (2003). doi:10.1103/RevModPhys.75.607

[25] S. G. Zhou, J. Meng, and P. Ring et al., Neutron halo in deformed nuclei. Phys. Rev. C **82**, 011301(R) (2010). doi:10.1103/PhysRevC.82.011301

[26] L. Li, J. Meng, and P. Ring et al., Deformed relativistic Hartree Bogoliubov theory in continuum. Phys. Rev. C **85**, 024312 (2012). doi:10.1103/PhysRevC.85.024312

[27] N. Michel, W. Nazarewicz, and M. Ploszajczak et al., Gamow shell model description of neutron rich nuclei. Phys. Rev. Lett. **89**, 042502 (2002). doi:10.1103/PhysRevLett.89.042502

[28] N. Michel, W. Nazarewicz, and M. Ploszajczak et al., Antibound states and halo formation in the Gamow Shell Model. Phys. Rev. C **74**, 054305 (2006). doi:10.1103/PhysRevC.74.054305

[29] N. Michel, K. Matsuyanagi, and M. Stoitsov, Gamow-Hartree-Fock-Bogoliubov Method: Representation of quasiparticles with Berggren sets of

wave functions. Phys. Rev. C **78**, 044319 (2008). doi:10.1103/PhysRevC.78.044319

[30] J. Meng, *Relativistic Density Functional for Nuclear Structure* (World Scientific, Singapore, 2016).

[31] N. Li, M. Shi, and J. Y. Guo et al., Probing Resonances of the Dirac Equation with Complex Momentum Representation. Phys. Rev. Lett. **117**, 062502 (2016). doi:10.1103/PhysRevLett.117.062502

[32] X. X. Shi, Q. Liu, and J. Y. Guo et al., Pseudospin and spin symmetries in single particle resonant states in Pb isotopes. Phys. Lett. B **801**, 135174 (2020). doi:10.1016/j.physletb.2019.135174

[33] Q. Liu, Y. Zhang, and J. Y. Guo, Pseudospin symmetry in resonant states and its dependence on the shape of potential. Phys. Lett. B **824**, 136829 (2022). doi:10.1016/j.physletb.2021.136829

[34] K. M. Ding, M. Shi, and J. Y. Guo et al., Resonant-continuum relativistic mean-field plus BCS in complex momentum representation. Phys. Rev. C **98**, 014316 (2018). doi:10.1103/PhysRevC.98.014316

[35] X. N. Cao, Q. Liu, and Z. M. Niu et al., Systematic studies of the influence of single-particle resonances on neutron halo and skin in the relativistic-mean-field and complex-momentum-representation methods. Phys. Rev. C **99**, 024314 (2019). doi:10.1103/PhysRevC.99.024314

[36] X. N. Cao, K. M. Ding, and M. Shi et al., Exploration of the exotic structure in Ce isotopes by the relativistic point-coupling model combined with complex momentum representation. Phys. Rev. C **102**, 044313 (2020). doi:10.1103/PhysRevC.102.044313

[37] Z. Fang, M. Shi, and J. Y. Guo et al., Probing resonances in the Dirac equation with quadrupole-deformed potentials with the complex momentum representation method. Phys. Rev. C **95**, 024311 (2017). doi:10.1103/PhysRevC.95.024311

[38] Y. X. Luo, K. Fossez, and Q. Liu et al., Role of quadrupole deformation and continuum effects in the “island of inversion” nuclei ^{28,29,31}F Phys. Rev. C **104**, 014307 (2021).

[39] X. W. Wang, and J. Y. Guo, Research on deformed exotic nuclei by relativistic mean field theory in complex momentum representation. Phys. Rev. C **104**, 044315 (2021). doi:10.1103/PhysRevC.104.044315

[40] Y. X. Luo, Q. Liu, and J. Y. Guo, Research on exotic nuclei in deformed relativistic mean-field theory plus BCS in complex momentum representation. Phys. Rev. C **108**, 024320 (2023). doi:10.1103/PhysRevC.108.024320

[41] Y. X. Luo, Q. Liu, and J. Y. Guo, Exploration of the ground state properties of neutron-rich sodium isotopes using the deformed relativistic mean field theory in complex momentumrepresentations with BCS pairings. Chin. Phys. C **48**, 044103 (2024). doi:10.1088/1674-1137/ad1fe3

[42] B. V. Pritychenko, T. Glasmacher, and P. D. Cottle, et al., Role of intruder configurations in ^{26,28}Ne and ^{30,32}Mg. Phys. Lett. B **461**, 322 (1999). doi:10.1016/S0370-2693(99)00850-3

[43] H. Scheit, O. Niedermaier, and M. Pantea et al., First results on inbeam gamma spectroscopy of neutron rich Na and Mg isotopes at REX-ISOLDE. Nucl. Phys. A **746**, 96 (2004). doi:10.1016/j.nuclphysa.2004.09.126

[44] B. V. Pritychenko, T. Glasmacher, and P. D. Cottle et al., Structure of the “island of inversion” nucleus ^{33}Mg. Phys. Rev. C **65**, 061304(R) (2002). doi:10.1103/PhysRevC.65.061304

[45] A. Chaudhuri, C. Andreoiu, and T. Brunner et al., Evidence for the extinction of the $N = 20$ neutron-shell closure for ^{32}Mg from direct mass measurements. Phys. Rev. C **88**, 054317 (2013). doi:10.1103/PhysRevC.88.054317

[46] N. Kitamura, K. Wimmer, and N. Shimizu et al., Structure of ^{30}Mg explored via in-beam γ-ray spectroscopy. Phys. Rev. C **102**, 054318 (2020). doi:10.1103/PhysRevC.102.054318

[47] K. Wimmer, T. Kroll, and R. Krcken et al., Discovery of the shape coexisting 0^+ state in ^{32}Mg by a two neutron transfer reaction. Phys. Rev. Lett. **105**, 252501 (2010). doi:10.1103/PhysRevLett.105.252501

[48] R. Kanungo, C. Nociforo, and A. Prochazka et al., Structure of ^{33}Mg sheds new light on the $N = 20$ island of inversion. Phys. Lett. B **685**, 253 (2010). doi:10.1016/j.physletb.2010.02.008

[49] S. Nummela, F. Nowacki, and P. Baumann et al., Intruder features in the island of inversion: The case of ^{33}Mg. Phys. Rev. C **64**, 054313 (2001). doi:10.1103/PhysRevC.64.054313

[50] V. Tripathi, S. L. Tabor, and P. F. Mantica et al., Intruder Configurations in the A=33 Isobars: ^{33}Mg and ^{33}Al. Phys. Rev. Lett. **101**, 142504 (2008). doi:10.1103/PhysRevLett.101.142504

[51] D. Bazin, N. Aoi, and H. Baba et al., Spectroscopy of ^{33}Mg with knockout reactions. Phys. Rev. C **103**, 064318 (2021). doi:10.1103/PhysRevC.103.064318

[52] U. Datta, A. Rahaman, and T. Aumann et al., Direct experimental evidence for a multiparticle-hole ground state configuration of deformed ^{33}Mg. Phys. Rev. C **94**, 034304 (2016). doi:10.1103/PhysRevC.94.034304

[53] K. Yoneda, H. Sakurai, and T. Gomi et al., Deformation of ^{34}Mg studied via in-beam γ -ray spectroscopy using radioactive-ion projectile fragmentation. Phys. Lett. B **499**, 233 (2001). doi:10.1016/S0370-2693(01)00025-9

[54] H. Iwasaki, T. Motobayashi, and H. Sakurai, et al., Large collectivity of ^{34}Mg. Phys. Lett. B **522**, 227 (2001). doi:10.1016/S0370-2693(01)01244-8

[55] A. Gade, P. Adrich, and D. Bazin et al., Spectroscopy of ^{36}Mg: Interplay of Normal and Intruder Configurations at the Neutron-Rich Boundary of the ‘Island of Inversion’. Phys. Rev. Lett. **99**, 072502 (2007). doi:10.1103/PhysRevLett.99.072502

[56] P. Doornenbal, H. Scheit, and S. Takeuchi et al., In-Beam γ-Ray Spectroscopy of ^{34,36,38}Mg: Merging the $N = 20$ and $N = 28$ Shell Quenching. Phys. Rev. Lett. **111**, 212502 (2013). doi:10.1103/PhysRevLett.111.212502

[57] H. L. Crawford, P. Fallon, and A. O. Macchiavelli et al., First Spectroscopy of the Near Drip-line Nucleus ^{40}Mg. Phys. Rev. Lett. **122**, 052501 (2019). doi:10.1103/PhysRevLett.122.052501

[58] E. Caurier, F. Nowacki, and A. Poves, Merging of the islands of inversion at $N = 20$ and $N = 28$. Phys. Rev. C **90**, 014302 (2014). doi:10.1103/PhysRevC.90.014302

[59] M. Takechi, S. Suzuki, and D. Nishimura et al., Evidence of halo structure in ^{37}Mg observed via reaction cross sections and intruder orbitals beyond the island of inversion. Phys. Rev. C **90**, 061305(R) (2014). doi:10.1103/PhysRevC.90.061305

[60] N. Kobayashi, T. Nakamura, and Y. Kondo et al., Observation of a ρ-Wave One-Neutron Halo Configuration in Mg^{37}. Phys. Rev. Lett. **112**, 242501 (2014). doi:10.1103/PhysRevLett.112.242501

[61] Z. Ren, Z. Y. Zhu, and Y. H. Cai et al., Relativistic mean-field study of Mg isotopes. Phys. Lett. B **380**, 241 (1996). doi:10.1016/0370-2693(96)00462-5

[62] X. X. Sun, and S. G. Zhou, Rotating deformed halo nuclei and shape decoupling effects. Sci. Bull. **66**, 2072 (2021). doi:10.1016/j.scib.2021.07.005

[63] K. Y. Zhang, D. Y. Wang, and S. Q. Zhang, Effects of pairing, continuum, and deformation on particles in the classically forbidden regions for Mg isotopes. Phys. Rev. C **100**, 034312 (2019). doi:10.1103/PhysRevC.100.034312

[64] M. A. Khan, M. Hasan, and S. H. Mondal et al., Hyperspherical three-body model calculation for the bound and resonant states of the neutron dripline nuclei ^{42,44}Mg using isospectral potential. Nucl. Phys. A **1015**, 122316 (2021). doi:10.1016/j.nuclphysa.2021.122316

[65] A. Bohr, and B. R. Mottelson, *Nuclear Structure* (Benjamin, New York, 1969), Vol. I.

[66] D. Vretenar, A. V. Afanasjev, and G. A. Lalazissis et al., Relativistic Hartree Bogoliubov theory: static and dynamic aspects of exotic nuclear structure. Phys. Rep. **409**, 101 (2005). doi:10.1016/j.physrep.2004.10.001

[67] P. Ring, Relativistic mean field in finite nuclei. Prog. Part. Nucl. Phys. **37**, 193 (1996). doi:10.1016/0146-6410(96)00054-3

[68] G. A. Lalazissis, J. König, and P. Ring, A New parametrization for the Lagrangian density of relativistic mean field theory. Phys. Rev. C **55**, 540 (1997).doi:10.1103/PhysRevC.55.540

[69] G. Audi, F. G. Kondev, and M. Wang et al., The NUBASE2016 evaluation of nuclear properties. Chin. Phys. C **41**, 030001 (2017). doi:10.1088/1674-1137/41/3/030001

[70] W. J. Huang, G. Audi, and M. Wang et al., The AME2016 atomic mass evaluation (I). Evaluation of input data; and adjustment procedures. Chin. Phys. C **41**, 030002 (2017). doi:10.1088/1674-1137/41/3/030002

[71] M. Wang, G. Audi, and F. G. Kondev et al., The AME2016 atomic mass evaluation (II). Tables, graphs and references. Chin. Phys. C **41**, 030003 (2017). doi:10.1088/1674-1137/41/3/030003

[72] F. G. Kondev, M. Wang, and W. J. Huang et al., The NUBASE2020 evaluation of nuclear physics properties. Chin. Phys. C **45**, 030001 (2021). doi:10.1088/1674-1137/abddae

[73] W. J. Huang, M. Wang, and F. G. Kondev et al., The AME 2020 atomic mass evaluation (I). Evaluation of input data, and adjustment procedures. Chin. Phys. C **45**, 030002 (2021). doi:10.1088/1674-1137/abddb0

[74] M. Wang, W. J. Huang, and F. G. Kondev et al., The AME 2020 atomic mass evaluation (II). Tables, graphs and references. Chin. Phys. C **45**, 030003 (2021). doi:10.1088/1674-1137/abddaf

[75] W. h. Long, J. Meng, and N. Van Giai et al., New effective interactions in RMF theory with nonlinear terms and density dependent meson nucleon coupling. Phys. Rev. C **69**, 034319 (2004). doi:10.1103/PhysRevC.69.034319